

## Reconstructing the phase diagram of iron in the terapascal region via the statistical moment method

Tran Dinh Cuong <sup>1,\*</sup> and Anh D. Phan <sup>1,2</sup>

<sup>1</sup>*Faculty of Materials Science and Engineering, Phenikaa University, Yen Nghia, Ha Dong, Hanoi 12116, Vietnam*

<sup>2</sup>*Phenikaa Institute for Advanced Study (PIAS), Phenikaa University, Yen Nghia, Ha Dong, Hanoi 12116, Vietnam*



(Received 31 July 2023; revised 5 October 2023; accepted 9 October 2023; published 20 October 2023)

Recently, astronomers have reached a significant milestone on a journey of Universe exploration with more than 5400 confirmed exoplanets. Therefore determining the physical properties of minerals in the terapascal area has become an urgent mission to gain insights into exoplanetary dynamics and evolution. Herein, we develop a theoretical model to obtain a more reliable picture of the ultrahigh-pressure structural transformation in iron, which is the most prominent metal in the core of super-Earths, gas giants, and ice giants. First, we revisit the previously computed hcp-fcc boundary under extreme conditions between 3 and 7 TPa. Available *ab initio* data for the ground-state energy are utilized to construct the Rydberg pairwise potential for iron. On that basis, the statistical moment method is improved to calculate the total vibrational free energy without enormous computational workloads. Our analyses reveal that the widely employed quasiharmonic approximation is insufficient to capture the hcp-fcc phase-transition behaviors of iron. The primary reason is that the lack of inversion symmetry creates strong odd-order anharmonic effects, thereby enhancing the thermodynamic stability of the hcp structure. Second, we extend the modified work-heat equivalence principle to deduce the melting quantities from the Holzapfel equation-of-state parameters up to 10 TPa. Our steep melting lines accord fully with the state-of-the-art static measurements, dynamic experiments, and *ab initio* simulations. In particular, we observe that the melting gradient of hcp iron is always higher than the adiabatic slope of liquid iron. This difference has a profound geophysical implication for the core solidification and the magnetic-field generation of super-Earths. Finally, we perform numerical calculations for the Hugoniot and isentropic profiles. Our theoretical predictions would facilitate designing future multishock and ramp-wave studies to uncover the mystery of extrasolar worlds.

DOI: [10.1103/PhysRevB.108.134111](https://doi.org/10.1103/PhysRevB.108.134111)

### I. INTRODUCTION

Searching for planets and life outside our Solar System has aroused great interest [1–3] since Wolszczan and Frail announced the first discovery of two exoplanets around the pulsar PSR 1257 + 12 in January 1992 [4]. After three decades of tireless efforts, there are now up to 5463 confirmed celestial bodies in NASA’s Exoplanet Archive [5]. Although these extrasolar objects show enormous diversity, scientists can classify them into four principal groups with the following proportions [6]: (i) terrestrial (3.6%), (ii) super-Earth (30.3%), (iii) Neptune-like (34.4%), and (iv) gas giant (31.7%). Group (i) includes small worlds of rock with the planetary radius  $R_p$  between  $0.8R_\oplus$  and  $1.25R_\oplus$ , where  $R_\oplus = 6371$  km is Earth’s radius. Similarly, group (ii) consists of potentially rocky exoplanets, but the upper limit of  $R_p$  increases to  $2R_\oplus$ . According to geodynamic models [7–9], minerals can be strongly compressed up to 4 TPa at the center of super-Earths. In contrast to the first two groups, group (iii) is built on observational data for gaseous worlds around Neptune’s size ( $2R_\oplus \leq R_p \leq 6R_\oplus$ ). Huger gaseous exoplanets ( $R_p \geq 6R_\oplus$ ) are found in group (iv), where it is notable that the central pressure can exceed 7 TPa [10–12].

The mentioned impressive figures have promoted intensive studies on materials’ properties in harsh environments to advance our understanding of physical processes in exoplanetary interiors [13–15]. In that context, the phase diagram of iron has grabbed particular attention due to its pivotal role in elucidating the architecture, dynamics, history, and fate of exoplanetary cores [16–19]. For example, correct information about the melting transition of iron is required to answer the following questions [20]. How does the molten core of super-Earths crystallize? When does the core crystallization begin and finish? Is this process efficient in powering and maintaining the magnetosphere—one of the most critical factors for the habitability of super-Earths [21]? Besides, it is well-known that the crystalline structure of materials affects their solubility in metallic hydrogen fluid [22–24]. Thus intimate knowledge of the solid-solid structural transformation in iron is indispensable for considering the erosion of dense cores and the evolution of dilute ones in gas giants [25].

For the above reasons, many experimental approaches have been introduced to capture the phase relations of iron. Conventionally, experimentalists employ the diamond-anvil-cell (DAC) technique [26] to recreate extreme conditions in Earth-sized or smaller exoplanets. This useful static-compression method allows continuous access to a pressure-temperature ( $P$ - $T$ ) domain ranging from 0 TPa and 300 K to 0.377 TPa and 5700 K [27]. On that basis, the phase boundaries of iron can

\*cuong.trandinh@phenikaa-uni.edu.vn

be directly determined in the  $P$ - $T$  space [28–30]. It is possible to generate higher pressures by applying shock-wave (SW) and ramp-wave (RW) techniques [31]. The physical behaviors of iron samples are governed by the Rankine-Hugoniot equation in SW experiments [32], whereas the correlation between  $P$  and  $T$  is nearly isentropic in RW measurements [33]. By combining these dynamic approaches, Smith *et al.* [34] demonstrated that the stability field of hcp iron would span at least from 0.06 to 1.4 TPa. Likewise, Kraus *et al.* [35] investigated the melting phenomenon of iron up to 1 TPa, thereby estimating the length of dynamo action in super-Earths. However, there is considerable controversy about available experimental results [36–38]. At Earth’s inner-core pressure of 0.33 TPa, the disagreement between the lowest measured melting temperature (4850 K [39]) and the highest one (7600 K [40]) reaches 36%, far beyond DAC, SW, and RW acceptable error ranges. Additionally, it is conspicuous that the current experimental accessibility ( $P \sim 1.4$  TPa [34]) is still insufficient to probe the phase transition in Jupiter-sized exoplanets ( $P \sim 7$  TPa [31]). Hence, the true phase diagram of iron remains an intriguing mystery to the scientific community.

Apart from experiments, using density functional theory (DFT) [41] is a common strategy for studying the phase-transition behaviors of iron. This powerful first-principles method enables evaluating ionic, electronic, and magnetic contributions to the thermodynamic stability without empirical adjustable parameters. Notably, based on DFT computations, Stixrude [42] considered the phase relations of iron up to 100 TPa. At 0 K, a bcc-hcp-fcc-bcc sequence of lattice structures was observed during isothermal squeezing [42]. While the bcc-hcp structural change at 0.011 TPa was attributed to ferromagnetic effects, the hcp-fcc transition at 6 TPa and the fcc-bcc transition at 38.3 TPa were respectively explained by  $4s - 3d$  electron transfer and  $3p - 3d$  hybridization [42]. These findings were fairly consistent with the cold-DFT calculations of Pickard and Needs [43]. Unfortunately, in the high-temperature regime, Stixrude’s phase diagram [42] remains questionable. Stixrude [42] only described the thermal fluctuation of iron atoms via the quasi-harmonic approximation (QHA), which may occasion an incorrect prediction of solid-solid phase boundaries similar to the case of beryllium [44,45] and magnesium oxide [46,47]. Moreover, since the melting process of iron was studied via the Lindemann law for vibrational instability [48], its melting temperature may be substantially underestimated [49,50]. It is challenging to address the mentioned problems via DFT because of the prohibitive computational cost of anharmonic simulations, such as molecular dynamics (MD) and thermodynamic integration (TI).

Remarkably, recent years have witnessed the emergence of some promising tools for handling anharmonic excitations, including the statistical moment method (SMM) [51–56], the temperature-dependent effective potential (TDEP) [57], the stochastic self-consistent harmonic approximation (SSCHA) [58], and the compressive sensing lattice dynamics (CSLD) [59]. Among them, the SMM is the simplest model. The SMM core idea is to utilize the quantum density matrix to establish a recurrence formula for atomic-displacement moments [60]. Accordingly, the total vibrational free energy is

explicitly analyzed under various temperature-volume ( $T$ - $V$ ) conditions [51–56]. Unlike DFT-MD and DFT-TI simulations, SMM analyses can be quickly performed even on a personal computer [51–56]. Having the SMM at hand, Hung *et al.* [51,52] determined the thermal expansivity of metals and semiconductors at the quantitative level. Cuong and Phan [53] successfully solved the violation of Arrhenius’s law for silver, copper, nickel, molybdenum, and tungsten vacancies. The underlying correlation among lattice symmetry, intrinsic anharmonicity, and physical stability was also clarified for titanium, zirconium, and beryllium [54,55]. In particular, Cuong *et al.* [56] explored an intimate connection between the high-pressure melting curve of iron and its room-temperature equation of state (EoS) via the work-heat equivalence principle (WHEP) [61]. Their SMM-WHEP results [56] agreed quantitatively well with the latest DAC, SW, and RW data [35]. Nevertheless, Cuong *et al.* [56] could not capture the polymorphism of solid iron in the terapascal region due to the limitation of the semi-DFT pairwise potential used in their research. Furthermore, their theoretical calculations [56] were restricted to 4 TPa, almost half lower than Jupiter’s central pressure.

Herein, we improve the SMM model to acquire a better description of the structural transformation in iron up to 10 TPa. Because solid-solid coexistence lines below 0.1 TPa were unambiguously reported in previous experimental works [62], we do not revisit them in the present study. In addition, we ignore the presence of superionic bcc iron, which was discovered by the large-scale MD computations of Belonoshko *et al.* [63,64] under deep-Earth conditions. Although the liquidlike characteristics of the bcc phase help explain seismic observations satisfactorily [65,66], they conflict with DAC, SW, and RW shreds of evidence [34–37]. From 0.1 to 1.4 TPa, no bcc signatures have been confidently experimentally detected in pure iron samples [34–37]. Instead, experimentalists have only found the existence of the hcp structure before melting [34–37]. Computationally, the newest TI investigations of Sun *et al.* [67] also indicated that the bcc phase stability should not be due to iron alone. If the bcc structure does exist in Earth’s core, it should be produced by alloying iron with nickel, sulfur, or silicon [68–70]. Despite a fascinating issue, evaluating the influence of impurities on the phase diagram of iron is beyond the scope of our current research.

## II. THEORETICAL BACKGROUND

### A. Vibrational Helmholtz free energy

In the SMM theory [51–56], an arbitrary iron atom is modeled by a three-dimensional quantum oscillator possessing the atomic mass  $m_0$ , the Einstein-like frequency  $\omega_E$ , and the displacement  $u_\zeta$  along the  $\zeta$ -Cartesian axis. Relying on the Leibfried-Ludwig expansion [71], we can represent the difference between the potential energy  $E$  of the selected atom and its ground-state energy  $E_0$  via

$$E - E_0 = 3 \left( \frac{k}{2} \langle u_\zeta^2 \rangle + \beta \langle u_\zeta \rangle \langle u_\eta^2 \rangle + \gamma_1 \langle u_\zeta^4 \rangle + \gamma_2 \langle u_\zeta^2 \rangle \langle u_\eta^2 \rangle \right),$$

$$\zeta \neq \eta = x, y, \text{ or } z, \quad (1)$$

where the angle bracket  $\langle \dots \rangle$  denotes the average value of the enclosed quantity in the thermodynamic equilibrium. Mathematically, it is easy to see that  $k$ ,  $\beta$ ,  $\gamma_1$ , and  $\gamma_2$  are given by

$$k = \left( \frac{\partial^2 E}{\partial u_\zeta^2} \right)_{\text{eq}}, \quad \beta = \left( \frac{\partial^3 E}{\partial u_\zeta \partial u_\eta^2} \right)_{\text{eq}},$$

$$\gamma_1 = \frac{1}{24} \left( \frac{\partial^4 E}{\partial u_\zeta^4} \right)_{\text{eq}}, \quad \gamma_2 = \frac{1}{4} \left( \frac{\partial^4 E}{\partial u_\zeta^2 \partial u_\eta^2} \right)_{\text{eq}}. \quad (2)$$

They can be further expressed as a function of  $V$ , as detailed in the Supplemental Material of Refs. [53,55]. From a physical perspective,  $k = m_0 \omega_E^2$  serves as the quasiharmonic force constant,  $\beta$  indicates the odd-order anharmonicity (OAH), and  $\gamma_1$  and  $\gamma_2$  characterize the even-order anharmonicity (EAH). Note that all crystallographic information about iron is encoded in these vibrational coupling parameters. To facilitate subsequent SMM analyses, we set

$$\gamma = 4(\gamma_1 + \gamma_2), \quad K = k - \frac{\beta^2}{3\gamma},$$

$$\theta = k_B T, \quad X = \frac{\hbar \omega_E}{2\theta} \coth \left( \frac{\hbar \omega_E}{2\theta} \right), \quad (3)$$

where  $k_B$  and  $\hbar$  are the Boltzmann constant and the reduced Planck one, respectively.

Equations (2) and (3) allow us to infer the mean atomic displacement  $\langle u_\zeta \rangle$  from the force-balance condition as [56]

$$\langle u_\zeta \rangle = y_0 - \frac{\beta}{3\gamma} + A_1 \frac{\beta k}{3\gamma} \left[ 1 - \frac{2\beta^2}{9\gamma k} - \frac{2\gamma\theta}{k^2} (X - 1) \right]. \quad (4)$$

One of the most exciting things about the SMM is that we can directly link the first-order moment  $\langle u_\zeta \rangle$  to its high-order counterparts via [51,54]

$$\langle u_\zeta^2 \rangle = \langle u_\zeta \rangle^2 + \theta A_1 + \frac{\theta}{k} (X - 1), \quad (5)$$

$$\langle u_\zeta^4 \rangle = \langle u_\zeta \rangle^4 + \theta \left[ 6A_1 + \frac{1}{k} (X - 1) \right] \langle u_\zeta \rangle^2$$

$$+ 8\theta^2 A_2 \langle u_\zeta \rangle + \theta^2 A_1 \left[ 3A_1 + \frac{1}{k} (X - 1) \right]. \quad (6)$$

Based on the iterative method of Tang and Hung [60], the explicit form of  $y_0$ ,  $A_1$ , and  $A_2$  is written by [56]

$$y_0 = \sqrt{\frac{2\gamma\theta^2}{3K^3}} A,$$

$$A_1 = \frac{1}{K} \left[ 1 + \frac{2\gamma^2\theta^2}{K^4} \left( 1 + \frac{X}{2} \right) (1 + X) \right],$$

$$A_2 = \frac{1}{2Ky_0} \left[ \frac{1}{3K} (1 - X) - \frac{1}{K} - \frac{y_0^2}{\theta} \right], \quad (7)$$

where

$$A = 1 + \frac{X}{2} + \sum_{n=2}^6 \frac{\gamma^n \theta^n}{K^{2n}} a_n. \quad (8)$$

Details about the  $X$  dependence of the dimensionless coefficient  $a_n$  were reported in earlier SMM literature [72–74].

After determining all atomic-displacement moments appearing in Eq. (1), it is feasible to get the vibrational Helmholtz free energy  $F_{\text{vib}}$  without strenuous computational efforts [51–56]. Specifically,  $F_{\text{vib}}$  is decomposed into

$$F_{\text{vib}} = E_0 + F_{\text{QHA}} + F_{\text{OAH}} + F_{\text{EAH}}. \quad (9)$$

According to quantum statistical physics [75], the quasiharmonic contribution  $F_{\text{QHA}}$  is quantified by

$$F_{\text{QHA}} = \frac{3}{2} \hbar \omega_E + 3\theta \ln \left[ 1 - \exp \left( -\frac{\hbar \omega_E}{\theta} \right) \right], \quad (10)$$

where the first term arises from the zero-point motion and the second term stems from thermal excitations. Meanwhile, the anharmonic components  $F_{\text{OAH}}$  and  $F_{\text{EAH}}$  are deduced from the following thermodynamic integrals [75]

$$F_{\text{OAH}} = 3 \int_0^\beta \langle u_\zeta \rangle \langle u_\eta^2 \rangle d\beta, \quad (11)$$

$$F_{\text{EAH}} = 3 \int_0^{\gamma_1} \langle u_\zeta^4 \rangle d\gamma_1 + 3 \int_0^{\gamma_2} \langle u_\zeta^2 \rangle \langle u_\eta^2 \rangle d\gamma_2. \quad (12)$$

Consequently, we obtain the general analytical expression for  $F_{\text{vib}}$  in the solid state as [54,55]

$$F_{\text{vib}} = E_0 + \frac{3}{2} \hbar \omega_E + 3\theta \ln \left[ 1 - \exp \left( -\frac{\hbar \omega_E}{\theta} \right) \right]$$

$$+ \frac{\theta^2}{K^2} [3\gamma_2 X^2 - \gamma_1 (X + 2)]$$

$$+ \frac{2\theta^3}{K^4} (X + 2) [2\gamma_2^2 X - 3\gamma_1 (\gamma_1 + 2\gamma_2) (X + 1)]$$

$$+ \frac{3\beta\theta^2}{K} \left[ \frac{\gamma(X + 2)}{3K^3} \right]^{\frac{1}{2}}$$

$$+ 3\beta\theta^3 \left\{ \left[ \frac{\gamma(X + 2)}{3K^3} \right]^{\frac{3}{2}} + \frac{2k\gamma}{K^6} \beta \right\}. \quad (13)$$

In the high-temperature limit ( $T \gg \hbar \omega_E / 2k_B$ ), because  $X$  is approximately equal to 1, Eq. (13) is reduced to

$$F_{\text{vib}} = E_0 + \frac{3}{2} \hbar \omega_E + 3\theta \ln \left( \frac{\hbar \omega_E}{\theta} \right) + \frac{3\theta^2}{K^2} (\gamma_2 - \gamma_1)$$

$$+ \frac{12\theta^3}{K^4} [\gamma_2^2 - 3\gamma_1 (\gamma_1 + 2\gamma_2)] + \frac{3\beta\theta^2}{K} \left( \frac{\gamma}{K^3} \right)^{\frac{1}{2}}$$

$$+ 3\beta\theta^3 \left[ \left( \frac{\gamma}{K^3} \right)^{\frac{3}{2}} + \frac{2k\gamma}{K^6} \beta \right]. \quad (14)$$

Equation (13) is seen as a decisive factor in shedding light on the impact of atomic fluctuations on the physical properties of iron. To ensure the accuracy and efficiency of SMM free-energy calculations, we need a suitable interatomic-potential model for  $E_0$ . How to meet this requirement? A clear-cut answer is provided in the next subsection.

## B. Interatomic potential

### 1. DFT-based Rydberg model

Today, numerous interatomic potentials for iron are publicly available in online repositories (e.g., the NIST database

[76,77]). Principally, they are derived from the embedded atom method (EAM) [78]—a modern theory of metallic bonding. The EAM enables physicists to describe pairwise and multibody interactions simultaneously at the atomistic level. In addition, it is possible to include angular forces by applying the MEAM [79,80]—a modified version of the EAM. These positive aspects make the EAM an appealing choice for investigating the physical characteristics of iron via classical MD simulations [81–85].

Nonetheless, there are two main reasons why the EAM is inappropriate for our current study. First, most EAM potentials are built on experimental or computational results at around 0 TPa. Therefore they are likely invalid in severe environments. Partay [86] adopted the nested sampling technique to examine the reliability of four prevalent EAM models, including Ackland97 [87], Mendeleev03 [88], Chamati06 [89], and Marinica07 [90]. Unfortunately, none of these models succeeded in reproducing the measured phase diagram of

iron between 0 and 0.1 TPa [86]. Whereas Ackland97 [87], Chamati06 [89], and Marinica07 [90] caused a vast overestimation of the melting temperature, Mendeleev03 [88] led to the vanishing of the hcp structure. Second, Cuong and Phan [53,55] showed that employing the EAM would make the analytical form of  $k$ ,  $\beta$ ,  $\gamma_1$ , and  $\gamma_2$  very complicated, thereby decelerating the running of SMM programs. It should be stressed that our ultimate goal is to decipher the terapascal phase relations of iron with minimal computational time and cost. Hence, although the NIST repository has a few EAM potentials developed from high-pressure DFT data [91], we cannot choose them for our SMM calculations.

Notably, in recent years, the SMM community has seen the appearance of several two-body potentials  $\varphi_i(r_i)$  originating from DFT cold energy curves [55,56]. According to the Leibfried-Ludwig theory [71], if we have  $E_0 = \frac{1}{2} \sum_i \varphi_i(r_i)$ , the vibrational coupling parameters will be expressed by

$$\begin{aligned}
 k &= \frac{1}{2} \sum_i \left[ \frac{d^2 \varphi_i}{dr_i^2} \frac{\zeta_i^2}{r_i^2} + \frac{d\varphi_i}{dr_i} \left( \frac{1}{r_i} - \frac{\zeta_i^2}{r_i^3} \right) \right], \\
 \beta &= \frac{1}{2} \sum_i \left[ \frac{d^3 \varphi_i}{dr_i^3} \frac{\zeta_i \eta_i^2}{r_i^3} + \frac{d^2 \varphi_i}{dr_i^2} \left( \frac{\zeta_i}{r_i^2} - \frac{3\zeta_i \eta_i^2}{r_i^4} \right) + \frac{d\varphi_i}{dr_i} \left( \frac{3\zeta_i \eta_i^2}{r_i^5} - \frac{\zeta_i}{r_i^3} \right) \right], \\
 \gamma_1 &= \frac{1}{48} \sum_i \left[ \frac{d^4 \varphi_i}{dr_i^4} \frac{\zeta_i^4}{r_i^4} + \frac{d^3 \varphi_i}{dr_i^3} \left( \frac{6\zeta_i^2}{r_i^3} - \frac{6\zeta_i^4}{r_i^5} \right) + \frac{d^2 \varphi_i}{dr_i^2} \left( \frac{15\zeta_i^4}{r_i^6} - \frac{18\zeta_i^2}{r_i^4} + \frac{3}{r_i^2} \right) + \frac{d\varphi_i}{dr_i} \left( -\frac{15\zeta_i^4}{r_i^7} + \frac{18\zeta_i^2}{r_i^5} - \frac{3}{r_i^3} \right) \right], \\
 \gamma_2 &= \frac{1}{8} \sum_i \left[ \frac{d^4 \varphi_i}{dr_i^4} \frac{\zeta_i^2 \eta_i^2}{r_i^4} + \frac{d^3 \varphi_i}{dr_i^3} \left( \frac{\zeta_i^2}{r_i^3} + \frac{\eta_i^2}{r_i^3} - \frac{6\zeta_i^2 \eta_i^2}{r_i^5} \right) + \frac{d^2 \varphi_i}{dr_i^2} \left( -\frac{3\zeta_i^2}{r_i^4} - \frac{3\eta_i^2}{r_i^4} + \frac{15\zeta_i^2 \eta_i^2}{r_i^6} + \frac{1}{r_i^2} \right) \right. \\
 &\quad \left. + \frac{d\varphi_i}{dr_i} \left( \frac{3\zeta_i^2}{r_i^5} + \frac{3\eta_i^2}{r_i^5} - \frac{15\zeta_i^2 \eta_i^2}{r_i^7} - \frac{1}{r_i^3} \right) \right], \tag{15}
 \end{aligned}$$

where  $r_i$  is the separation between the selected atom and the  $i$ th one. As opposed to the EAM, Eq. (15) is mathematically straightforward and transparent. Thus the SMM computational efficiency is dramatically enhanced [55,56]. Besides, since the parametrization of  $E_0$  is performed over a broad volume range, Eq. (15) is well-suited to strongly compressed systems [55,56]. In the case of iron, Cuong *et al.* [56] handled Eq. (15) by the Morse function of Ye *et al.* [92] as

$$\varphi_i = D_M [e^{-2b_M(r_i - r_{0M})} - 2e^{-b_M(r_i - r_{0M})}], \tag{16}$$

where  $D_M = 0.6317$  eV was the dissociation energy,  $b_M^{-1} = 0.7089$  Å was the decay length, and  $r_{0M} = 2.6141$  Å was the equilibrium distance. The above approach helped Cuong *et al.* [56] to accurately regenerate the DFT-MD melting line [16] from 0 to 1.5 TPa at breakneck speed. However, Ye *et al.* [92] only used DFT outputs for bcc iron to determine the Morse parameters, so their potential failed to recreate the intersection between  $E_0^{\text{hcp}}(V^{\text{hcp}})$  and  $E_0^{\text{fcc}}(V^{\text{fcc}})$  profiles. In other words, Cuong *et al.* [56] could not access the hcp-fcc phase boundary of iron via Eq. (16).

What should we do to address this situation? The simplest strategy is to extend the idea of Ye *et al.* [92] and Cuong *et al.* [56] by adding the DFT information about hcp

and fcc structures to potential fitting procedures. Herein, we extract the necessary data for the ground-state energy from the linearized-augmented plane-wave (LAPW) simulations of Stixrude and Cohen [93]. Essentially, the LAPW [93] allows taking into account the contribution of core and valence electrons without approximating the shape of charge densities or crystal potentials. This outstanding advantage makes the LAPW one of the most precise DFT implementations [94]. To further improve the quality of SMM predictions, we replace Eq. (16) with the Rydberg function [95], which is

$$\varphi_i = -D_R [1 + b_R(r_i - r_{0R})] \exp[-b_R(r_i - r_{0R})]. \tag{17}$$

Similar to previous SMM works [55], the cutoff radius is selected as  $d\sqrt{3}$ , where  $d = (V\sqrt{2})^{\frac{1}{3}}$  is the nearest neighbor distance. Our fitted results for  $D_R$ ,  $b_R$ , and  $r_{0R}$  are fully reported in Table I.

## 2. Model validation

To validate the obtained Rydberg parameters, we perform numerical calculations for some typical thermodynamic and elastic properties of iron, which were thoroughly simulated and measured under intense compression. Because the

TABLE I. Our Rydberg parameters for hcp iron and fcc iron.

Phase	$D_R$ (eV)	$b_R$ ( $\text{\AA}^{-1}$ )	$r_{0R}$ ( $\text{\AA}$ )
hcp	0.524851	2.56479	2.52699
fcc	0.507905	2.53961	2.54703

standard thermal condition of 300 K is imposed, all SMM analyses are done within the QHA to save time.

We begin with the EoS  $P(V)$ , the Grüneisen parameter  $\gamma_G$ , and the volumetric thermal expansion coefficient  $\alpha$ . Thermodynamically, these quantities are defined by [75]

$$\begin{aligned}
 P &= -\left(\frac{\partial F_{\text{vib}}}{\partial V}\right)_T, \\
 \gamma_G &= -\frac{V}{\omega_E} \left(\frac{\partial \omega_E}{\partial V}\right)_T, \\
 \alpha &= \frac{1}{V} \left(\frac{\partial V}{\partial T}\right)_P.
 \end{aligned} \quad (18)$$

Figure 1 presents how  $P$ ,  $\gamma_G$ , and  $\alpha$  depend on  $V$ . Overall, there is a good agreement between the SMM-Rydberg and cutting-edge experimental/computational approaches [34,96–102]. Specifically, for the atomic volume, our SMM-Rydberg results only differ from the DFT outputs of Hakim *et al.* [97] by a maximum of  $0.18 \text{ \AA}^3$  throughout a wide pressure range from 0 to 10 TPa. A better consistency will be reached if Hakim *et al.* [97] add finite-temperature effects to their DFT EoS. For  $\gamma_G$  and  $\alpha$ , the difference between our

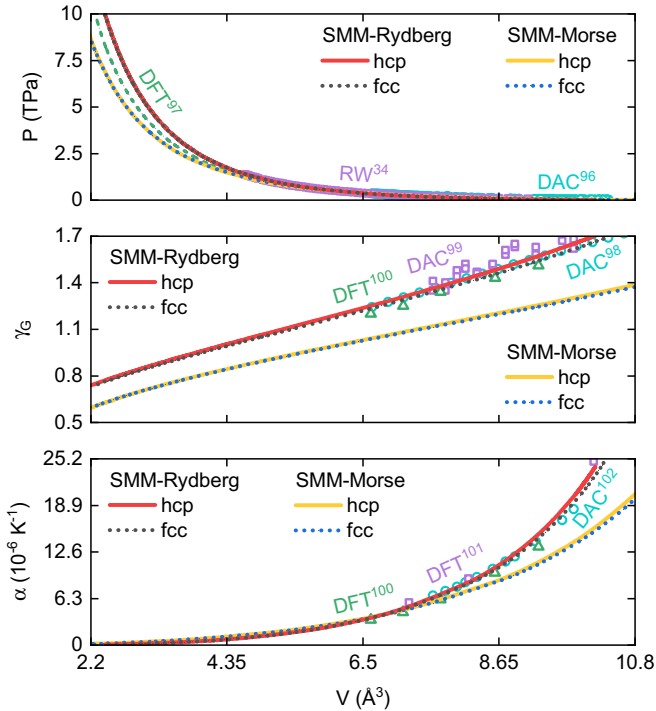


FIG. 1. The atomic-volume dependence of the pressure, the Grüneisen parameter, and the thermal expansivity given by SMM calculations, DFT simulations [97,100,101], and RW/DAC measurements [34,96,98,102].

TABLE II. Details about fitting parameters in Eq. (19).

Parameter	Type	Unit	hcp iron	fcc iron
$V_0$	Holzappel	$\text{\AA}^3$	10.1697	10.3038
$B_0$	Holzappel	GPa	245.0660	236.9228
$c_0$	Holzappel	None	1.9571	2.0360
$c_2$	Holzappel	None	2.3713	2.1203
$\gamma_0$	Al'tshuler	None	1.7029	1.6846
$\gamma_\infty$	Al'tshuler	None	0.5440	0.5305
$q$	Al'tshuler	None	1.1053	1.0789
$\alpha_0$	Anderson	$10^{-6} \text{ K}^{-1}$	24.1403	24.6609
$\delta_0$	Anderson	None	5.1554	5.1066
$\kappa$	Anderson	None	0.5633	0.5555

SMM-Rydberg analyses and the latest DFT computations of Bouchet *et al.* [100] is less than 7.5% at  $V = 6.6238 \text{ \AA}^3$ . It should be emphasized that our Rydberg potential is superior to the Morse potential of Ye *et al.* [92] in reproducing DAC and DFT reference data [34,96–102]. Therefore our quantum-mechanical calculations would be valuable for capturing how pressure, density, and temperature are distributed inside exoplanets [97]. To facilitate future geophysical studies, we parametrize SMM-Rydberg outputs by the Holzappel EoS [103], the Al'tshuler function [104], and the Anderson model [105] as

$$\begin{aligned}
 P &= 3B_0\xi^{-5}(1-\xi)\exp[c_0(1-\xi)][1+c_2\xi(1-\xi)], \\
 \gamma_G &= \gamma_\infty + (\gamma_0 - \gamma_\infty)\xi^{3q}, \\
 \alpha &= \alpha_0 \exp\left[-\frac{\delta_0}{\kappa}(1-\xi^{3\kappa})\right],
 \end{aligned} \quad (19)$$

where  $\xi = (V/V_0)^{1/3}$ . Specific values of  $V_0$ ,  $B_0$ ,  $c_0$ ,  $c_2$ ,  $\gamma_0$ ,  $\gamma_\infty$ ,  $q$ ,  $\alpha_0$ ,  $\delta_0$ , and  $\kappa$  are listed in Table II.

Next, we focus on the sound-wave propagation in iron. Equation (19) helps us to quickly calculate the isothermal bulk modulus  $B_T$  and its adiabatic counterpart  $B_S$  by

$$\begin{aligned}
 B_T &= B_0\xi^{-5}\exp[c_0(1-\xi)]\{c_0c_2\xi^4 - 2c_2(c_0-1)\xi^3 \\
 &\quad + [c_0(c_2-1) - 6c_2]\xi^2 + (c_0+4c_2-4)\xi + 5\}, \\
 B_S &= B_T(1 + \alpha\gamma_G T).
 \end{aligned} \quad (20)$$

Meanwhile, the Young modulus  $Y$  of iron can be straightforwardly computed by adopting the Hung-Hai cylindrical method [106] as

$$Y = \frac{d}{A_1 S}, \quad (21)$$

where  $S = \frac{1}{2}\pi d^2$  is the effective cross-section inferred from the low-pressure Poisson ratio of 0.23 [102]. According to the classical theory of elasticity [107], the shear modulus  $\mu$  is associated with  $B_S$  and  $Y$  via

$$\mu = \frac{3B_S Y}{9B_S - Y}. \quad (22)$$

Table III shows excellent accordance between our estimations based on Eqs. (20) to (22) and the recent DFT simulations of Martorell *et al.* [108] at Earth's center ( $P = 0.36$  TPa). After having accurate information about elastic moduli, we

TABLE III. The elastic moduli of iron deduced from SMM approximations and DFT computations [108] at 0.36 TPa.

Method	Phase	$B_S$ (GPa)	$\mu$ (GPa)
SMM-Rydberg	hcp	1690	630
DFT [108]	hcp	1590	655
SMM-Rydberg	fcc	1666	627
DFT [108]	fcc	1598	650

can readily consider the compressional-wave velocity  $v_p$  and the shear-wave one  $v_s$  by

$$v_p = \sqrt{\frac{3B_S + 4\mu}{3\rho}},$$

$$v_s = \sqrt{\frac{\mu}{\rho}}. \quad (23)$$

where  $\rho = m_0/V$  is the mass density.

Figure 2 presents  $v_p$  and  $v_s$  as a function of  $\rho$ . In general, our SMM-Rydberg approach can quantitatively explain the significant growth of  $v_p$  and  $v_s$  during isothermal squeezing. Whereas  $v_p$  climbs about 4.25-fold in a mass-density region from 9 to 38 g cm<sup>-3</sup>,  $v_s$  increases about 2.90 times in the same condition. Our theoretical curves lie very close to DAC and DFT benchmark points [100,109–111]. The largest relative error is merely 5.9% in the experimentally accessible area. Additionally, we notice a marked improvement in calculating the mechanical characteristics of iron when replacing Eq. (16) with Eq. (17). These positive outcomes confirm the reliability of the Rydberg potential developed by our group.

Geophysically, our analyses for sound-wave propagation at high densities would be meaningful for predicting the chemical composition of planetary interiors. For instance, it is conspicuous that the sound velocities of hcp iron are appreciably faster than those of Earth's inner core.

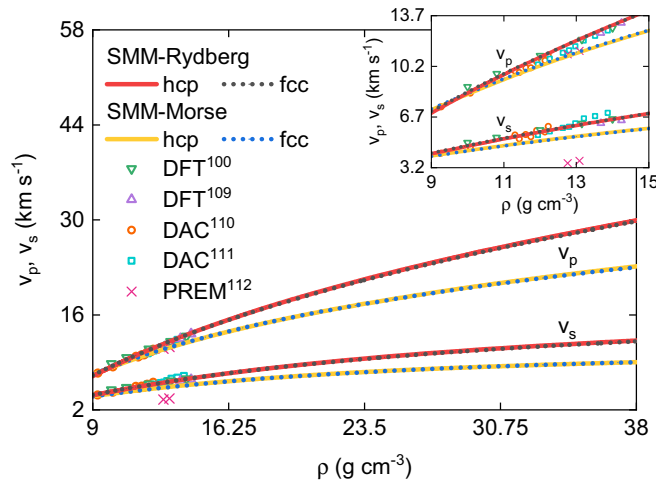


FIG. 2. Correlations between the mass density and the sound velocity of iron gained from SMM, DFT [100,109], and DAC [110,111] methods. Seismic data [112] for the Earth's inner core are plotted for comparison. (Inset) The experimentally accessible domain is zoomed in to clarify the effectiveness of the Rydberg potential.

At  $\rho = 13.0885$  g cm<sup>-3</sup>, the preliminary reference Earth model of Dziewonski and Anderson [112] provides  $v_s = 3.6678$  km s<sup>-1</sup>, about 40.5% lower than our SMM-Rydberg value of  $v_s = 6.1600$  km s<sup>-1</sup>. This deficit suggests that the deepest part of our home planet contains a substantial amount of hydrogen, oxygen, and carbon. Interestingly, the mentioned impurities can rapidly diffuse like an ionic liquid in the lattice space of hcp iron, thereby softening Earth's inner core [113]. Some other elements (e.g., nickel, silicon, and sulfur) should also be considered to achieve the best match between mineral-physics and seismic studies [114].

### III. RESULTS AND DISCUSSION

#### A. hcp-fcc transition

Having constructed an appropriate interatomic-potential model for SMM calculations, let us investigate how iron changes its crystalline structure from the hcp type to the fcc one via the Gibbs energy difference  $\Delta G$  as

$$\Delta G = F_{\text{vib}}^{\text{hcp}} - F_{\text{vib}}^{\text{fcc}} + P(V^{\text{hcp}} - V^{\text{fcc}}) + \Delta F_{\text{el}}. \quad (24)$$

If  $\Delta G$  has a negative value, iron will exist with the hcp form. In contrast, if  $\Delta G$  is positive, the fcc phase will be stabilized. The hcp-fcc transition occurs when  $\Delta G$  equals zero. It is worth noting that  $\Delta F_{\text{el}}$  symbolizes an electronic correction, which keeps us from overestimating the hcp field. As demonstrated by Stixrude [42], electronic excitations favor the stability of the fcc structure. The fundamental reason is that the  $ABCABC\dots$  packing sequence of fcc iron creates a higher electronic density of states than the  $ABAB\dots$  arrangement of hcp iron at the Fermi level [115]. For simplicity, we quantify  $\Delta F_{\text{el}}$  by the well-known Sommerfeld approximation, which is

$$\Delta F_{\text{el}} = e_0[(V^{\text{hcp}})^{\gamma_e^{\text{hcp}}} - (V^{\text{fcc}})^{\gamma_e^{\text{fcc}}}]T^2. \quad (25)$$

Since  $\gamma_e^{\text{hcp}}$  serves as the electronic Grüneisen parameter, it is reasonable to fix  $\gamma_e^{\text{hcp}} = 2$ . This figure is commonly used in experiments on the thermal EoS of hcp iron [116] and its alloys [117]. Additionally, relying on the linear muffin-tin orbital method, Boness *et al.* [118] indicated that  $\gamma_e^{\text{hcp}}$  and  $\gamma_e^{\text{fcc}}$  would be almost identical. Sherman also arrived at the same conclusion after carrying out full-potential LAPW calculations [119]. These pieces of evidence enable us to approximate  $\gamma_e^{\text{fcc}} \approx \gamma_e^{\text{hcp}} = 2$ . On that basis, we find  $e_0 = 6.9935 \times 10^{-6}$  meV Å<sup>-6</sup> K<sup>-2</sup> by utilizing the DFT-QHA hcp-fcc-liquid triple point of Stixrude [42] at 3.634 TPa. Another thing to note is that we ignore the impact of magnetisms on  $\Delta G$  because of the vanishing of spins at  $P < 0.2$  TPa [120].

Our numerical results for the hcp-fcc phase boundary  $T_s(P_s)$  of iron are presented in Fig. 3 with the aid of the VESTA software [121]. Overall,  $P_s$  undergoes a dramatic decrease during heating [Fig. 3(a)]. In the ground state, we realize that hcp iron transforms to fcc iron at 6.492 TPa, which concurs completely with earlier DFT predictions ( $6 \leq P_s \leq 7$  TPa [42,43]). When QHA thermal effects are included,  $P_s$  drops considerably by a factor of 1.93 from 0 to 18 000 K. As illustrated in Fig. 3(b), our SMM-QHA computations are quantitatively consistent with the DFT-QHA simulations of Stixrude [42]. The discrepancy between the above approaches does not exceed 4.3% in the elevated-temperature regime

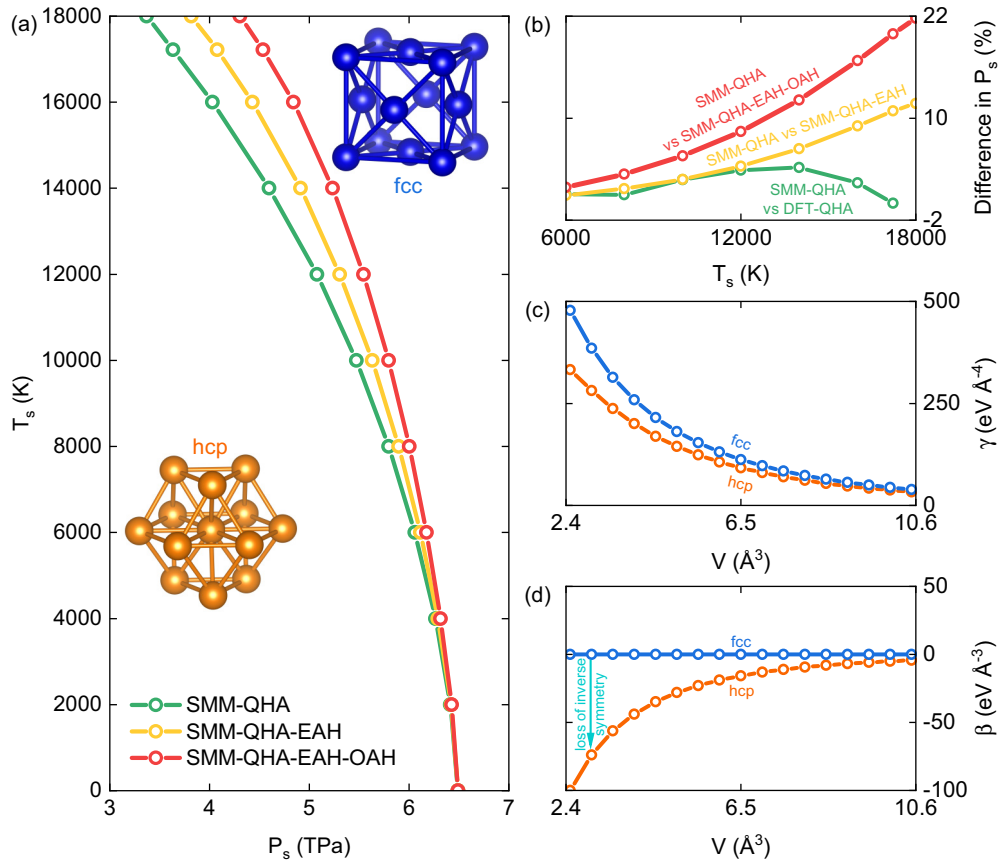


FIG. 3. (a) The hcp-fcc coexistence curve of iron yielded by various SMM approximations for the vibrational Helmholtz free energy. The visualization of hcp iron and its fcc counterpart is done via the VESTA software [121]. (b) The relative error between quasi-harmonic and anharmonic SMM calculations for the hcp-fcc transition pressure. The DFT outputs of Stixrude [42] are added to verify the accuracy of SMM results. (c) The EAH parameter  $\gamma$  of hcp and fcc phases as a function of the atomic volume. (d) The impact of the atomic volume on the OAH parameter  $\beta$  of hcp and fcc lattices.

( $T_s \geq 6000$  K). A better consensus may be achieved if we take into account the contribution of many-body interactions to the Helmholtz free energy.

Remarkably, even though the QHA is widely applied owing to its convenience, this treatment is inadequate for deciphering the structural transformation of iron. Our quantum-statistical analyses reveal that the appearance of intrinsic anharmonicity forcefully straightens up the hcp-fcc coexistence line [Fig. 3(a)]. At  $T_s = 18000$  K,  $P_s$  taken from the quasi-harmonic SMM is up to 21.8% smaller than  $P_s$  extracted from the fully anharmonic SMM [Figure 3(b)]. Our physical picture is supported by state-of-the-art DFT calculations for beryllium [44,45] and magnesium oxide [46,47].

A critical question to be answered is why anharmonic excitations can lead the hcp region to expand to such a degree. It is often expected that the influence of nonlinear atomic vibrations on the hcp-fcc transition of iron is not too big due to the similarity in the coordination number of hcp and fcc structures [42,122]. From the SMM point of view, these arguments are only valid if we neglect the odd-order anharmonicity. Fig. 3(c) shows that  $\gamma^{\text{fcc}}$  is comparable to  $\gamma^{\text{hcp}}$ . Hence, no surprising difference in  $P_s$  is recorded when even-order anharmonic effects appear alone. The widest gap between SMM-QHA and SMM-QHA-EAH boundaries is 0.448 TPa. However, the inclusion of odd-order anharmonic terms alters

the situation significantly. As depicted in Fig. 3(d), while the OAH excitations of fcc iron are entirely suppressed by the symmetric properties of perfect cubic lattice ( $\beta = 0$ ), those of hcp iron are drastically amplified by the destruction of inverse symmetry around the selected atom ( $\beta < 0$ ). It is easy to see from Eqs. (13) and (24) that the mentioned phenomenon reduces  $\Delta G$  dramatically. In other words, the thermodynamic stability of the hcp phase is markedly enhanced by odd-order anharmonic contributions stemming from inverse asymmetries. Our theoretical findings are bolstered by cutting-edge DFT simulations for aluminum, copper, and nickel with symmetric and asymmetric close-packed structures [123,124]. For future reference, we fit SMM data by [125]

$$T_s = s_1 \left( 1 + \frac{P_s - s_2}{s_3} \right)^{s_4} \exp[-s_5(P_s - s_2)], \quad (26)$$

where  $s_1 = 0.5$  K,  $s_2 = 6.492$  TPa,  $s_3 = -6.98625 \times 10^{-7}$  TPa,  $s_4 = 0.725017$ , and  $s_5 = -0.161302$  TPa $^{-1}$  are the Kechin parameters.

Another equally crucial question is what geophysical implications the hcp-field expansion has. To answer this thoroughly, we need to know where hcp, fcc, and liquid systems can coexist on the phase diagram. One of the most viable strategies for pinpointing the hcp-fcc-liquid triple point is to compare the hcp-fcc profile with the melting profile [44–47].

Consequently, a deep understanding of melting behaviors in the terapascal area is indispensable. Details about the high-pressure melting process of iron are disclosed in the subsequent subsection.

### B. Solid-liquid transition

Herein, we adopt the modified WHEP (mWHEP) model of Cuong *et al.* [55,56], which is well-suited to describe the melting phenomenon of pure metals and ionic compounds [126]. Fundamentally, the crystallization of molten samples can happen via two different mechanisms: heat release and mechanical deformation. Thus there is an equivalence between the heat energy lost during isobaric cooling and the mechanical work obtained during isothermal squeezing. Relying on this idea, we can directly connect the melting curve  $T_m(P_m)$  with the room-temperature EoS by

$$T_m(P_m) = T_m(0) \left[ 1 + (B'_0 - 1) \sqrt{-\frac{6}{B_0} \int_1^\xi P(\xi') \xi'^2 d\xi'} \right], \quad (27)$$

where  $B'_0$  is the pressure derivative of the isothermal bulk modulus at 0 TPa. Applying Eq. (20) yields  $B_0^{\text{hcp}} = 5.8856$  and  $B_0^{\text{fcc}} = 5.7709$ , which are very close to the DFT calculations of Hakim *et al.* [97] ( $B'_0 = 5.7$ ) and the RW measurements of Smith *et al.* [34] ( $B'_0 = 5.64$ ). In addition, the reference melting temperature is taken from the machine-learning program of Hong as  $T_m^{\text{hcp}}(0) = 1750$  K [127]. As demonstrated by Cuong *et al.* [55,56], the mWHEP accelerates computational processes rapidly while maintaining an accuracy comparable to the two-phase approach. Its validity range primarily depends on the quality of the EoS used for integration [55,56]. Accordingly, we combine Eq. (19) with Eq. (27) to ensure that the mWHEP works effectively in harsh environments up to 10 TPa.

Figure 4(a) shows the melting line of hcp iron under deep-planetary conditions. On the experimental side, there are three controversial scenarios for the hcp-liquid transition: (i) low  $T_m$ , (ii) intermediate  $T_m$ , and (iii) high  $T_m$ . The first scenario was proposed by Boehler [39] in 1993. The pioneering DAC experiments of Boehler suggested that  $T_m$  would slowly grow to  $4850 \pm 200$  K at 0.33 TPa [39]. This result was lately reaffirmed by Aquilanti *et al.* [128] and Basu *et al.* [129]. Unfortunately, whereas the DAC measurements of Boehler [39] and Aquilanti *et al.* [128] may be severely affected by the diffusion of carbon atoms from diamond anvils, those of Basu *et al.* [129] may be negatively influenced by the nonlinear deformation of iron samples [130,131]. The second scenario was introduced by Jackson *et al.* [132] and Zhang *et al.* [133], who found  $T_m = 5700 \pm 200$  K at Earth's inner-core boundary. This finding was strengthened by recent DAC research of Sinmyo *et al.* [30] ( $T_m = 5500 \pm 220$  K). Nevertheless, metrological problems related to thermal pressures may cause Jackson *et al.* [132] and Zhang *et al.* [133] to underestimate the melting point of iron [130]. Besides, the DAC information supplied by Sinmyo *et al.* [30] may be inaccurate because of temperature-sensor issues [131]. The last scenario was produced by Anzellini *et al.* [134], Morard *et al.* [130], and

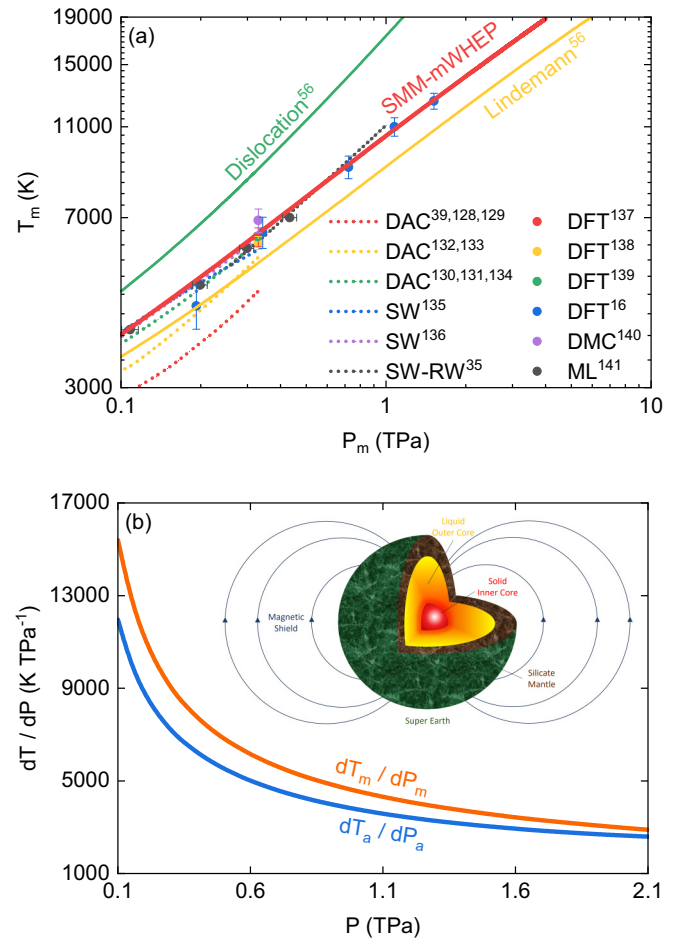


FIG. 4. (a) Our SMM-mWHEP outputs and previously measured/simulated results [16,35,39,56,128–141] for the hcp-liquid boundary of iron. DMC and ML stand for diffusion Monte Carlo and machine learning, respectively. (b) Comparison between the melting gradient and the adiabatic slope of iron along the SMM-mWHEP melting curve. Since  $dT_a/dP_a$  is markedly lower than  $dT_m/dP_m$ , the molten core of super-Earths would undergo bottom-up solidification, which is advantageous for generating the magnetic field.

Hou *et al.* [131]. Their DAC data [130,131,134] indicated that iron would possess a relatively steep melting curve with  $T_m = 6230 \pm 500$  K at  $P_m = 0.33$  TPa. This melting behavior was also recorded in a series of modern dynamic-compression experiments by Li *et al.* [135] ( $T_m = 5950 \pm 400$  K), Turneure *et al.* [136] ( $T_m \sim 6400$  K), and Kraus *et al.* [35] ( $T_m = 6230 \pm 540$  K).

On the computational side, most existing works support the view of Anzellini *et al.* [134], Morard *et al.* [130], and Hou *et al.* [131]. Specifically, our SMM-mWHEP model predicts that  $T_m$  would experience a sharp growth to 6470 K at the base of Earth's outer core. This number is in line with DFT-TI calculations [137,138] ( $T_m = 6350 \pm 300$  K and  $T_m = 6170 \pm 200$  K), DFT-MD simulations [139] ( $T_m = 6370 \pm 100$  K), diffusion Monte Carlo computations [140] ( $T_m = 6900 \pm 400$  K), and machine-learning investigations [141] ( $T_m = 6253 \pm 170$  K). The above agreement continues to be maintained even when  $P_m$  rises to 1.5 TPa—the

highest pressure reported in DFT studies on molten iron [16]. Conspicuously, our theoretical profile passes through all of the DFT-MD data points of Bouchet *et al.* [16] within error bars. Furthermore, there is an excellent consistency between our mWHEP analyses and the newest SW-RW measurements of Kraus *et al.* [35]. At 1 TPa, we obtain  $T_m = 10\,514$  K, which perfectly matches Kraus's result of  $T_m = 11\,087 \pm 800$  K [35]. It should be stressed that this consensus cannot be established via conventional one-phase approaches [56], such as the Lindemann criterion [142] or the dislocation-mediated melting theory [143]. Therefore we firmly believe that employing Eq. (27) is one of the most straightforward and effective ways to model the melting properties of iron.

Geophysically, our findings would be practical for elucidating the core solidification and the magnetic-field generation of super-Earths. There has been a long-standing debate about whether super-Earth cores crystallize from the bottom up or the top down [20]. If the bottom-up crystallization happens, super-Earths may possess a magnetic shield similar to our home planet, which protects organic life forms from the dangerous effects of cosmic radiation over a long period [17]. On the other hand, if the top-down crystallization occurs via the Mars-like snowflake mechanism, sustaining the magnetosphere of super-Earths for a long time may be a major challenge [18]. To resolve the mentioned controversy, we compare the melting gradient  $dT_m/dP_m$  of solid iron with the adiabatic slope  $dT_a/dP_a$  of liquid iron along the solid-liquid boundary. While  $dT_m/dP_m$  is inferred from our SMM-mWHEP code,  $dT_a/dP_a$  is deduced from the DFT-TI Python code of Li *et al.* [144]. The greatest benefit of these codes is that they can quickly provide reliable information about iron in the terapascal domain without much extrapolation. As shown in Fig. 4(b),  $dT_m/dP_m$  is always larger than  $dT_a/dP_a$  between 0.1 and 2.1 TPa. This deviation implies that super-Earths have a solid inner core due to bottom-up freezing.

Notably, when the inner core expands, it promotes turbulent motions in surrounding fluids by releasing light elements [145–147]. This process takes chief responsibility for powering dynamo actions. In that context, determining the crystalline structure of iron is essential since it is easier to exclude impurities from the hcp phase than its fcc counterpart [148]. Based on Eqs. (26) and (27), we discover that anharmonic excitations move the hcp-fcc-liquid triple point to a new position at  $T_m = 18\,842$  K and  $P_m = 3.9965$  TPa. Interestingly, the value of  $P_m$  almost coincides with the upper limit of super-Earth pressures ( $P = 4$  TPa [31]). This result suggests the dominance of hcp iron in the inner core of rocky exoplanets having  $1.25R_\oplus \leq R_p \leq 2R_\oplus$ . Hence, the release of light components is actively facilitated. In other words, the core solidification of super-Earths is expected to be efficient in driving the vigorous convection of liquid iron alloys, thereby maintaining the magnetosphere successfully. These predictions raise hopes of detecting the signatures of life beyond our home planet.

Figure 5 shows the influence of compression on the melting transition of fcc iron. We choose  $T_m^{\text{fcc}}(0) = 1765.6$  K to guarantee that hcp-liquid, hcp-fcc, and fcc-liquid boundaries cross at 3.9965 TPa. In general, the melting characteristics of fcc iron are pretty much the same as those of hcp iron. When

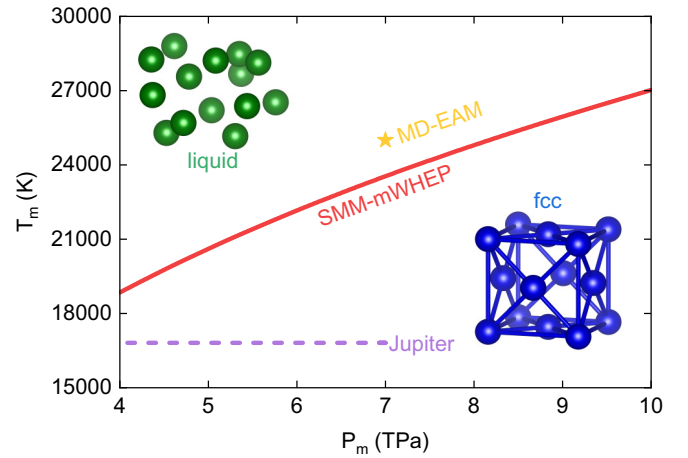


FIG. 5. Pressure effects on the melting temperature of fcc iron predicted by the SMM-mWHEP and the MD-EAM. *Ab initio* calculations for the thermal distribution in Jupiter's core are added for comparison [10].

$P_m$  increases to 10 TPa,  $T_m$  climbs sharply to 27024 K. The SMM-mWHEP melting tendency is reinforced by MD-EAM two-phase simulations in our Ref. [149]. At  $P_m = 7$  TPa, the MD-EAM yields  $T_m \sim 25000$  K, which is quite close to the SMM-mWHEP output of  $T_m = 23542$  K.

Our numerical results for fcc iron can be utilized to provide a deeper insight into the internal dynamics of gaseous worlds. Take Jupiter as an example. It is clear to see that its thermal profile [10] sits entirely below our SMM-mWHEP melting curve. Thus this gas giant may own a dense core made of fcc iron principally. However, according to Wahl *et al.* [23], the physical properties of fcc iron are strongly favorable for its dissolution in liquid metallic hydrogen. The above phenomenon causes Jupiter's dense core to fall into thermodynamic disequilibrium. While the iron core is gradually eroded, the hydrogen shell is enriched in heavy elements to form a dilute core [25]. Our physical picture promises to offer a better theoretical background for interpreting the gravitational-moment data from the JUNO probe [150].

### C. Hugoniot and isentrope

As discussed in Secs. III A and III B, the presence of fcc iron profoundly impacts geodynamic processes inside exoplanetary bodies. Consequently, we look forward to seeing more experimental works in the fcc regime. To aid in developing future experiments, we clarify the temperature variation of iron samples under dynamic loading via fully anharmonic SMM calculations.

Let us begin with the principal Hugoniot plot  $T_H(P_H)$ —a base for building dynamic compression measurements. The Rankine-Hugoniot relation is written by [32]

$$(U_{\text{vib}} - U_{\text{init}}) + \frac{1}{2}(P + P_{\text{init}})(V - V_{\text{init}}) = 0, \quad (28)$$

where the subscript “init” represents the initial state. Thermodynamically, the internal energy  $U_{\text{vib}}$  is associated with the

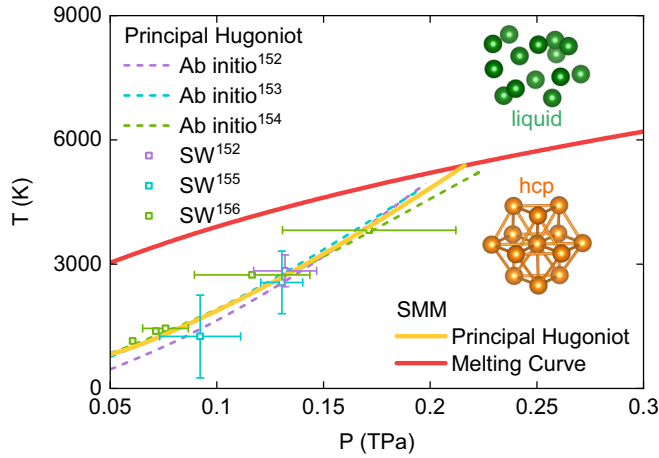


FIG. 6. SMM, *ab initio* [152–154], and SW [152,155,156] results for the principal Hugoniot. The SMM-mWHEP melting line is included to highlight how quickly iron heats up during single-shock compression.

Helmholtz free energy  $F_{\text{vib}}$  by [75]

$$U_{\text{vib}} = F_{\text{vib}} - T \left( \frac{\partial F_{\text{vib}}}{\partial T} \right)_V. \quad (29)$$

To find  $U_{\text{init}}$  and  $V_{\text{init}}$ , we reapply the SMM scheme to ferromagnetic bcc iron. Incorporating the LAPW data of Stixrude and Cohen [93] into the Rydberg fitting procedure [95] gives us  $D_R = 0.539864$  eV,  $b_R = 2.27614$  Å<sup>-1</sup>, and  $r_{0R} = 2.60477$  Å. These potential parameters yield  $U_{\text{init}} = -3.94297$  eV and  $V_{\text{init}} = 11.14069$  Å<sup>3</sup> for the bcc phase under ambient conditions ( $P_{\text{init}} = 0$  TPa and  $T_{\text{init}} = 300$  K). Moreover, the bcc-hcp structural transformation is detected at 0.0175 TPa along a room-temperature isotherm. Our SMM analyses are in good accordance with the previous DAC experiments of Dewaele *et al.* [151].

Figure 6 shows the correlation between  $T_H$  and  $P_H$ . Overall,  $T_H$  rises steeply during single-shock squeezing. The observed trend is quantitatively consistent with the *ab initio* predictions of Harmand *et al.* [152], Sjoström *et al.* [153], and Wu *et al.* [154]. Furthermore, our principal Hugoniot line traverses most of the SW points of Harmand *et al.* [152], Ping *et al.* [155], and Torchio *et al.* [156] within experimental uncertainties. These excellent agreements reaffirm the reliability and flexibility of our analytical model. Note that we do not use the results of Brown and McQueen [157] for comparison because the sample purity was only 99% in their study. From our perspective, the Hugoniot data of Brown and McQueen [157] are suitable for steel rather than pure iron. Indeed, Huang *et al.* [158] conducted SW investigations into iron-carbon alloys and achieved almost flawless consistency with the Hugoniot plot of Brown and McQueen [157].

Remarkably, since the growth rate of  $T_H$  is too fast, our system quickly enters the melt phase at  $P_H = 0.2162$  TPa. Although this number agrees well with the SW measurements of Nguyen and Holmes [159] ( $P_H = 0.225 \pm 0.003$  TPa), it is far below the central pressure of super-Earths, gas giants, and ice giants [7–12]. Accordingly, using the single-shock method alone is insufficient to explore the solid core of exoplanets. To go beyond this limit, we can employ the

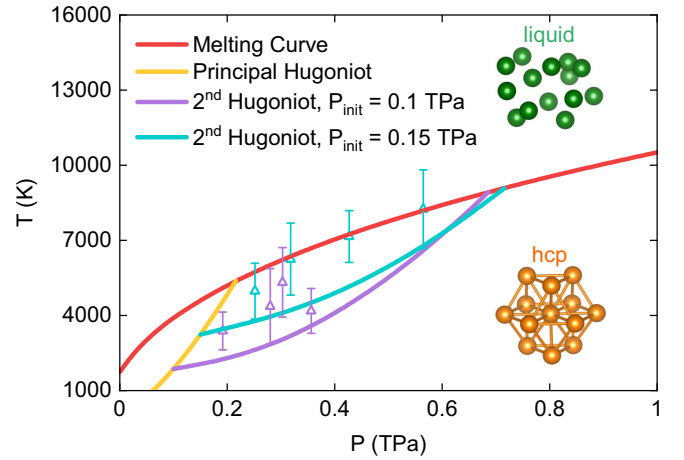


FIG. 7. The secondary Hugoniot of iron obtained from SMM analyses (solid lines) and SW measurements [155] (open triangles). The SMM-mWHEP solid-liquid boundary is plotted to illuminate the accessibility of the double-shock approach.

double-shock approach to generate the secondary Hugoniot  $T'_H(P'_H)$  [160]. Theoretically, the relation between  $T'_H$  and  $P'_H$  is described by Eq. (28), but the starting point is chosen from the principal Hugoniot instead of the ambient environment [32].

Figure 7 shows our numerical calculations for  $T'_H(P'_H)$ . It is conspicuous that the secondary Hugoniot is appreciably shallower than the principal Hugoniot. Therefore the double-shock technique enables probing a much wider solid region than the single-shock one. Specifically, if the second shock starts at  $P_{\text{init}} = 0.15$  TPa and  $T_{\text{init}} = 3239$  K, we can consider the physical characteristics of crystalline iron up to  $P'_H = 0.7159$  TPa and  $T'_H = 9089$  K. Our SMM approximations concur with the multishock experiments of Ping *et al.* [155]. A better concurrence may be attained if we add the influence of strain rates to our model. Recall that Ping *et al.* [155] compressed their systems at strain rates of  $10^6$ – $10^7$  s<sup>-1</sup>. This treatment may dramatically enhance the yield strength of iron samples [161]. The greater the yield strength was, the more plastic work was converted into heat [162]. Consequently, it is understandable why the experimental value of  $T'_H$  is higher than its theoretical counterpart.

Despite the above positive aspects, the double-shock approach is still restricted to the hcp domain. A viable solution to the problem is to develop the RW technique [33–35]. In the framework of the SMM, the RW temperature profile  $T_R(P_R)$  is estimated via the following isentropic criterion [75]

$$S_{\text{vib}} = - \left( \frac{\partial F_{\text{vib}}}{\partial T} \right)_V = \text{const}, \quad (30)$$

where  $S_{\text{vib}}$  is the entropy. Similar to  $P'_H$  and  $T'_H$ , the initial values of  $P_R$  and  $T_R$  are extracted from the principal Hugoniot. As shown in Fig. 8, the isentropes of iron are relatively flat. Hence, even when the terapascal pressure is applied, our system stays within the crystalline state. This advantage makes the RW one of the most promising tools for exploring the fcc area. Notwithstanding, because  $V^{\text{hcp}}$  and  $V^{\text{fcc}}$  are nearly identical (see Table II), the hcp-fcc transition may be undetectable via conventional  $P$ - $V$  measurements. Detecting

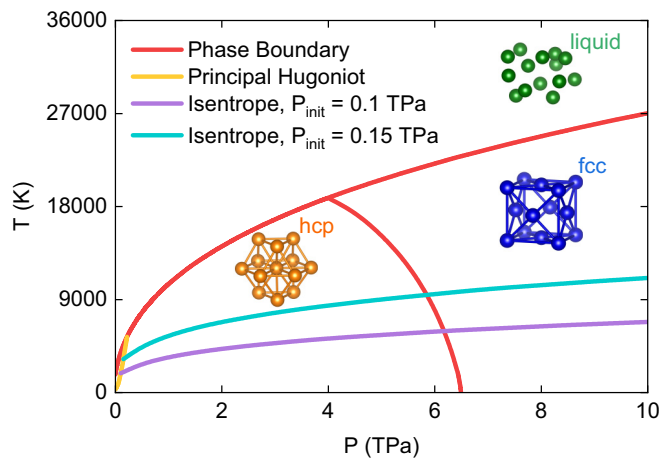


FIG. 8. SMM predictions of the temperature variation of iron during isentropic squeezing. The SMM phase diagram is added to elucidate why the ramp-compressed system can exist within the solid form up to ultrahigh pressures.

fcc signatures may require the development of more subtle observational methods, such as in situ x-ray diffraction and scattering [163,164].

#### IV. CONCLUSION

We have developed an anharmonic theory based on quantum-statistical mechanics to reconsider the phase-transition behaviors of iron in the terapascal regime. This

theory helps illuminate the underlying correlation among symmetric properties, vibrational excitations, and thermodynamic stabilities with extremely light computational workloads. On that basis, we have demonstrated that the breakdown of inverse symmetry would amplify odd-order anharmonic effects and then enlarge the hcp region. In other words, the hcp-fcc transition pressure reported in earlier *ab initio* literature was seriously underestimated as a corollary of using the quasiharmonic approximation. Moreover, we have uncovered that the melting characteristics of iron could be adequately explained via its equation-of-state parameters. A dramatic increase in the melting temperature has been recorded over an extensive pressure range between 0.1 and 10 TPa. The above conclusions have been positively reinforced by cutting-edge experimental and computational data. Thus our newly constructed phase diagram promises to be a valuable ingredient for modeling exoplanetary interiors. In addition, we have carefully analyzed the temperature change in iron crystals during the shock and ramp compression processes. Since all the necessary thermodynamic functions have been explicitly expressed, applying our analytical model to design dynamic experiments would be very convenient. We are eager to see more experimental results in the terapascal domain to better our understanding of extrasolar worlds.

#### ACKNOWLEDGMENT

We thank anonymous referees for their valuable comments and suggestions.

- 
- [1] J. J. Lissauer, R. I. Dawson, and S. Tremain, *Nature (London)* **513**, 336 (2014).
- [2] J. L. Christiansen, *Nat. Astron.* **6**, 516 (2022).
- [3] T. P. Greene, T. J. Bell, E. Ducrot, A. Dyrek, P. O. Lagage, and J. J. Fortney, *Nature (London)* **618**, 39 (2023).
- [4] A. Wolszczan and D. A. Frail, *Nature (London)* **355**, 145 (1992).
- [5] Latest data from NASA's Exoplanet Archive, <https://exoplanets.nasa.gov/discovery/> (accessed July 2023).
- [6] R. L. Akeson, X. Chen, D. Ciardi, M. Crane, J. Good, M. Harbut, E. Jackson, S. R. Kane, A. C. Laity, S. Leifer, M. Lynn, D. L. McElroy, M. Papin, P. Plavchan, S. V. Ramirez, R. Rey, K. von Braun, M. Wittman, M. Abajian, B. Ali *et al.* *Publ. Astron. Soc. Pac.* **125**, 989 (2013).
- [7] D. Valencia, R. J. O'Connell, and D. Sasselov, *Icarus* **181**, 545 (2006).
- [8] L. Zeng and S. B. Jacobsen, *Astrophys. J.* **837**, 164 (2017).
- [9] A. Boujibar, P. Driscoll, and Y. Fei, *J. Geophys. Res. Planets* **125**, e2019JE006124 (2020).
- [10] B. Militzer, *Phys. Rev. B* **87**, 014202 (2013).
- [11] N. Nettelmann, A. Becker, B. Holst, and R. Redmer, *Astrophys. J.* **750**, 52 (2012).
- [12] D. C. Swift, J. H. Eggert, D. G. Hicks, S. Hamel, K. Caspersen, E. Schwegler, G. W. Collins, N. Nettelmann, and G. J. Ackland, *Astrophys. J.* **744**, 59 (2012).
- [13] S. Mazevet, R. Musella, and F. Guyot, *Astron. Astrophys.* **631**, L4 (2019).
- [14] F. Coppari, R. F. Smith, J. H. Eggert, J. Wang, J. R. Rygg, A. Lazicki, J. A. Hawreliak, G. W. Collins, and T. S. Duffy, *Nat. Geosci.* **6**, 926 (2013).
- [15] Y. Fei, C. T. Seagle, J. P. Townsend, C. A. McCoy, A. Boujibar, P. Driscoll, L. Shulenburg, and M. D. Furnish, *Nat. Commun.* **12**, 876 (2021).
- [16] J. Bouchet, S. Mazevet, G. Morard, F. Guyot, and R. Musella, *Phys. Rev. B* **87**, 094102 (2013).
- [17] I. Bonati, M. Lasbleis, and L. Noack, *J. Geophys. Res. Planets* **126**, e2020JE006724 (2021).
- [18] D. J. Hemingway and P. E. Driscoll, *J. Geophys. Res. Planets* **126**, e2020JE006663 (2021).
- [19] S. C. Grant, T. Ao, C. T. Seagle, A. J. Porwitzky, J. P. Davis, K. R. Cochrane, D. H. Dolan, J. F. Lin, T. Ditmire, and A. C. Bernstein, *J. Geophys. Res. Solid Earth* **126**, e2020JB020008 (2021).
- [20] Y. Zhang and J. F. Lin, *Science* **375**, 146 (2022).
- [21] B. J. Foley and P. E. Driscoll, *Geochem. Geophys. Geosyst.* **17**, 1885 (2016).
- [22] H. F. Wilson and B. Militzer, *Phys. Rev. Lett.* **108**, 111101 (2012).
- [23] S. M. Wahl, H. F. Wilson, and B. Militzer, *Astrophys. J.* **773**, 95 (2013).

- [24] F. Gonzalez-Cataldo, H. F. Wilson, and B. Militzer, *Astrophys. J.* **787**, 79 (2014).
- [25] S. M. Wahl, W. B. Hubbard, B. Militzer, T. Guillot, Y. Miguel, N. Movshovitz, Y. Kaspi, R. Helled, D. Reese, E. Galanti, S. Levin, J. E. Connerney, and S. J. Bolton, *Geophys. Res. Lett.* **44**, 4649 (2017).
- [26] G. Shen and H. K. Mao, *Rep. Prog. Phys.* **80**, 016101 (2017).
- [27] S. Tateno, K. Hirose, Y. Ohishi, and Y. Tatsumi, *Science* **330**, 359 (2010).
- [28] A. Dewaele and L. Nataf, *Phys. Rev. B* **106**, 014104 (2022).
- [29] T. Komabayashi, Y. Fei, Y. Meng, and V. Prakapenka, *Earth Planet. Sci. Lett.* **282**, 252 (2009).
- [30] R. Sinmyo, K. Hirose, and Y. Ohishi, *Earth Planet. Sci. Lett.* **510**, 45 (2019).
- [31] T. S. Duffy and R. F. Smith, *Front. Earth Sci.* **7**, 23 (2019).
- [32] Y. B. Zel'dovich and Y. P. Raizer, *Physics of Shock Waves and High-temperature Hydrodynamic Phenomena* (Dover Publications, New York, 2002).
- [33] J. Wang, R. F. Smith, J. H. Eggert, D. G. Braun, T. R. Boehly, J. R. Patterson, P. M. Celliers, R. Jeanloz, G. W. Collins, and T. S. Duffy, *J. Appl. Phys.* **114**, 023513 (2013).
- [34] R. F. Smith, D. E. Fratanduono, D. G. Braun, T. S. Duffy, J. K. Wicks, P. M. Celliers, S. J. Ali, A. Fernandez-Panella, R. G. Kraus, D. C. Swift, G. W. Collins, and J. H. Eggert, *Nat. Astron.* **2**, 452 (2018).
- [35] R. G. Kraus, R. J. Hemley, S. J. Ali, J. L. Belof, L. X. Benedict, J. Bernier, D. Braun, R. E. Cohen, G. W. Collins, F. Coppari, M. P. Desjarlais, D. Fratanduono, S. Hamel, A. Krygier, A. Lazicki, J. Mcnaney, M. Millot, P. C. Myint, M. G. Newman, J. R. Rygg *et al.*, *Science* **375**, 202 (2022).
- [36] Y. Fei, *Science* **340**, 442 (2013).
- [37] R. Boehler and M. Ross, *Treatise on Geophysics*, 2nd ed. (Elsevier, Amsterdam, 2015), Vol. 2, p. 573.
- [38] I. C. Ezenwa and Y. Fei, *Geophys. Res. Lett.* **50**, e2022GL102006 (2023).
- [39] R. Boehler, *Nature (London)* **363**, 534 (1993).
- [40] Q. Williams, R. Jeanloz, J. Bass, B. Svendsen, and T. J. Ahrens, *Science* **236**, 181 (1987).
- [41] D. Alfe, *Treatise on Geophysics*, 2nd ed. (Elsevier, Amsterdam, 2015), Vol. 2, p. 369.
- [42] L. Stixrude, *Phys. Rev. Lett.* **108**, 055505 (2012).
- [43] C. J. Pickard and R. J. Needs, *J. Phys.: Condens. Matter* **21**, 452205 (2009).
- [44] J. W. Xian, J. Yan, H. F. Liu, T. Sun, G. M. Zhang, X. Y. Gao, and H. F. Song, *Phys. Rev. B* **99**, 064102 (2019).
- [45] J. Wu, F. Gonzalez-Cataldo, and B. Militzer, *Phys. Rev. B* **104**, 014103 (2021).
- [46] J. Bouchet, F. Bottin, V. Recoules, F. Remus, G. Morard, R. M. Bolis, and A. Benuzzi-Mounaix, *Phys. Rev. B* **99**, 094113 (2019).
- [47] F. Soubiran and B. Militzer, *Phys. Rev. Lett.* **125**, 175701 (2020).
- [48] J. J. Gilvarry, *Phys. Rev.* **102**, 308 (1956).
- [49] G. H. Wolf and R. Jeanloz, *J. Geophys. Res. Solid Earth* **89**, 7821 (1984).
- [50] J. Wu, F. Gonzalez-Cataldo, F. Soubiran, and B. Militzer, *J. Phys.: Condens. Matter* **34**, 144003 (2022).
- [51] K. Masuda-Jindo, V. V. Hung, and P. D. Tam, *Phys. Rev. B* **67**, 094301 (2003).
- [52] V. V. Hung, K. Masuda-Jindo, and P. T. M. Hanh, *J. Phys.: Condens. Matter* **18**, 283 (2006).
- [53] T. D. Cuong and A. D. Phan, *Phys. Chem. Chem. Phys.* **24**, 4910 (2022).
- [54] K. Masuda-Jindo, S. R. Nishitani, and V. VanHung, *Phys. Rev. B* **70**, 184122 (2004).
- [55] T. D. Cuong and A. D. Phan, *Phys. Chem. Chem. Phys.* **25**, 9073 (2023).
- [56] T. D. Cuong, N. Q. Hoc, N. D. Trung, N. T. Thao, and A. D. Phan, *Phys. Rev. B* **106**, 094103 (2022).
- [57] O. Hellman, P. Steneteg, I. A. Abrikosov, and S. I. Simak, *Phys. Rev. B* **87**, 104111 (2013).
- [58] I. Errea, M. Calandra, and F. Mauri, *Phys. Rev. B* **89**, 064302 (2014).
- [59] F. Zhou, W. Nielson, Y. Xia, and V. Ozolins, *Phys. Rev. B* **100**, 184308 (2019).
- [60] N. Tang and V. V. Hung, *Phys. Status Solidi B* **149**, 511 (1988).
- [61] J. Ma, W. Li, G. Yang, S. Zheng, Y. He, X. Zhang, X. Zhang, and X. Zhang, *Phys. Earth Planet. Inter.* **309**, 106602 (2020).
- [62] T. Komabayashi, *Crystals* **11**, 581 (2021).
- [63] A. B. Belonoshko, T. Lukinov, J. Fu, J. Zhao, S. Davis, and S. I. Simak, *Nat. Geosci.* **10**, 312 (2017).
- [64] A. B. Belonoshko, J. Fu, and G. Smirnov, *Phys. Rev. B* **104**, 104103 (2021).
- [65] A. B. Belonoshko, J. Fu, T. Bryk, S. I. Simak, and M. Mattesini, *Nat. Commun.* **10**, 2483 (2019).
- [66] A. B. Belonoshko, S. I. Simak, W. Olovsson, and O. Y. Vekilova, *Phys. Rev. B* **105**, L180102 (2022).
- [67] Y. Sun, M. I. Mendeleev, F. Zhang, X. Liu, B. Da, C. Z. Wang, R. M. Wentzcovitch, and K. M. Ho, *Geophys. Res. Lett.* **50**, e2022GL102447 (2023).
- [68] L. Vočadlo, D. Alfe, M. J. Gillan, I. G. Wood, J. P. Brodholt, and G. D. Price, *Nature (London)* **424**, 536 (2003).
- [69] L. Dubrovinsky, N. Dubrovinskaia, O. Narygina, I. Kantor, A. Kuznetsov, V. B. Prakapenka, L. Vitos, B. Johansson, A. S. Mikhaylushkin, S. I. Simak, and I. A. Abrikosov, *Science* **316**, 1880 (2007).
- [70] D. Ikuta, E. Ohtani, and N. Hirao, *Commun. Earth Environ.* **2**, 225 (2021).
- [71] G. Leibfried and W. Ludwig, *Solid State Phys.* **12**, 275 (1961).
- [72] D. D. Phuong, N. T. Hoa, V. V. Hung, D. Q. Khoa, and H. K. Hieu, *Eur. Phys. J. B* **89**, 84 (2016).
- [73] H. T. T. Vu, H. T. M. Pham, T. V. Nguyen, and H. K. Ho, *Eur. Phys. J. B* **90**, 65 (2017).
- [74] K. H. Ho, V. T. Nguyen, N. V. Nghia, N. B. Duc, V. Q. Tho, T. T. Hai, and D. Q. Khoa, *Curr. Appl. Phys.* **19**, 55 (2019).
- [75] M. E. Tuckerman, *Statistical Mechanics: Theory and Molecular Simulation* (Oxford University Press, New York, 2010).
- [76] C. A. Becker, F. Tavazza, Z. T. Trautt, and R. A. B. de Macedo, *Curr. Opin. Solid State Mater. Sci.* **17**, 277 (2013).
- [77] L. M. Hale, Z. T. Trautt, and C. A. Becker, *Modell. Simul. Mater. Sci. Eng.* **26**, 055003 (2018).
- [78] M. S. Daw, S. M. Foiles, and M. I. Baskes, *Mater. Sci. Rep.* **9**, 251 (1993).
- [79] E. Asadi, M. Asle Zaeem, S. Nouranian, and M. I. Baskes, *Phys. Rev. B* **91**, 024105 (2015).
- [80] S. Starikov, D. Smirnova, T. Pradhan, Y. Lysogorskiy, H. Chapman, M. Mrovec, and R. Drautz, *Phys. Rev. Mater.* **5**, 063607 (2021).
- [81] S. Plimpton, *J. Comput. Phys.* **117**, 1 (1995).

- [82] A. B. Belonoshko, R. Ahuja, and B. Johansson, *Phys. Rev. Lett.* **84**, 3638 (2000).
- [83] S. N. Luo, T. J. Ahrens, T. Cagin, A. Strachan, W. A. I. Goddard, and D. C. Swift, *Phys. Rev. B* **68**, 134206 (2003).
- [84] G. J. Ackland, M. I. Mendeleev, D. J. Srolovitz, S. Han, and A. V. Barashev, *J. Phys.: Condens. Matter* **16**, S2629 (2004).
- [85] W. J. Zhang, Z. Y. Liu, Z. L. Liu, and L. C. Cai, *Phys. Earth Planet. Inter.* **244**, 69 (2015).
- [86] L. B. Partay, *Comput. Mater. Sci.* **149**, 153 (2018).
- [87] G. J. Ackland, D. J. Bacon, A. F. Calder, and T. Harry, *Philos. Mag. A* **75**, 713 (1997).
- [88] M. I. Mendeleev, S. Han, D. J. Srolovitz, G. J. Ackland, D. Y. Sun, and M. Asta, *Philos. Mag.* **83**, 3977 (2003).
- [89] H. Chamati, N. I. Papanicolaou, Y. Mishin, and D. A. Papaconstantopoulos, *Surf. Sci.* **600**, 1793 (2006).
- [90] L. Malerba, M. C. Marinica, N. Anento, C. Bjorkas, H. Nguyen, C. Domain, F. Djurabekova, P. Olsson, K. Nordlund, A. Serra, D. Terentyev, F. Willaime, and C. S. Becquart, *J. Nucl. Mater.* **406**, 19 (2010).
- [91] Y. Sun, F. Zhang, M. I. Mendeleev, R. M. Wentzcovitch, and K. M. Ho, *Proc. Nat. Acad. Sci. USA* **119**, e2113059119 (2022).
- [92] Q. Ye, Y. Hu, X. Duan, H. Liu, H. Zhang, C. Zhang, L. Sun, W. Yang, W. Xu, Q. Cai, Z. Wang, and S. Jiang, *J. Synchrotron Radiat.* **27**, 436 (2020).
- [93] L. Stixrude and R. E. Cohen, *AIP Conf. Proc.* **309**, 911 (1994).
- [94] K. Lejaeghere, G. Bihlmayer, T. Bjorkman, P. Blaha, S. Blugel, V. Blum, D. Caliste, I. E. Castelli, S. J. Clark, A. D. Corso, S. de Gironcoli, T. Deutsch, J. K. Dewhurst, I. D. Marco, C. Draxl, M. Dułak, O. Eriksson, J. A. Flores-Livas, K. F. Garrity, L. Genovese *et al.*, *Science* **351**, aad3000 (2016).
- [95] Y. P. Varshni and F. J. Bloore, *Phys. Rev.* **129**, 115 (1963).
- [96] N. Hirao, Y. Akahama, and Y. Ohishi, *Matter Radiat. Extremes* **7**, 038403 (2022).
- [97] K. Hakim, A. Rivoldini, T. V. Hoolst, S. Cottenier, J. Jaeken, T. Chust, and G. Steinle-Neumann, *Icarus* **313**, 61 (2018).
- [98] L. S. Dubrovinsky, S. K. Saxena, N. A. Dubrovinskaia, S. Rekhi, and T. L. Bihan, *Am. Mineral.* **85**, 386 (2000).
- [99] C. A. Murphy, J. M. Jackson, W. Sturhahn, and B. Chen, *Geophys. Res. Lett.* **38** (2011).
- [100] J. Bouchet, F. Bottin, D. Antonangeli, and G. Morard, *J. Phys.: Condens. Matter* **34**, 344002 (2022).
- [101] X. Sha and R. E. Cohen, *Phys. Rev. B* **81**, 094105 (2010).
- [102] C. A. Murphy, J. M. Jackson, and W. Sturhahn, *J. Geophys. Res. Solid Earth* **118**, 1999 (2013).
- [103] W. B. Holzappel, M. Hartwig, and W. Sievers, *J. Phys. Chem. Ref. Data* **30**, 515 (2001).
- [104] L. V. Al'tshuler, S. E. Brusnikin, and E. A. Kuz'menkov, *J. Appl. Mech. Tech. Phys.* **28**, 129 (1987).
- [105] O. L. Anderson, H. Oda, and D. Isaak, *Geophys. Res. Lett.* **19**, 1987 (1992).
- [106] V. Van Hung and N. T. Hai, *Comput. Mater. Sci.* **14**, 261 (1999).
- [107] I. N. Sneddon and D. S. Berry, *The Classical Theory of Elasticity* (Springer, Berlin, 1958).
- [108] B. Martorell, J. Brodholt, I. G. Wood, and L. Vocablo, *Geophys. J. Int.* **202**, 94 (2015).
- [109] Z. Li and S. Scandolo, *Geophys. Res. Lett.* **49**, e2022GL101161 (2022).
- [110] E. Ohtani, Y. Shibazaki, T. Sakai, K. Mibe, H. Fukui, S. Kamada, T. Sakamaki, Y. Seto, S. Tsutsui, and A. Q. R. Baron, *Geophys. Res. Lett.* **40**, 5089 (2013).
- [111] D. Ikuta, E. Ohtani, H. Fukui, T. Sakai, D. Ishikawa, and A. Q. R. Baron, *Nat. Commun.* **13**, 7211 (2022).
- [112] A. M. Dziewonski and D. L. Anderson, *Phys. Earth Planet. Inter.* **25**, 297 (1981).
- [113] Y. He, S. Sun, D. Y. Kim, B. G. Jang, H. Li, and H. K. Mao, *Nature (London)* **602**, 258 (2022).
- [114] K. Hirose, B. Wood, and L. Vocablo, *Nat. Rev. Earth Environ.* **2**, 645 (2021).
- [115] F. Ducastelle and F. Cyrot-Lackmann, *J. Phys. Chem. Solids* **32**, 285 (1971).
- [116] Y. Fei, C. Murphy, Y. Shibazaki, A. Shahar, and H. Huang, *Geophys. Res. Lett.* **43**, 6837 (2016).
- [117] H. Huang, C. Leng, Q. Wang, G. Young, X. Liu, Y. Wu, F. Xu, and Y. Fei, *J. Geophys. Res. Solid Earth* **124**, 8300 (2019).
- [118] D. A. Boness, J. M. Brown, and A. K. McMahan, *Phys. Earth Planet. Inter.* **42**, 227 (1986).
- [119] D. M. Sherman, *Earth Planet. Sci. Lett.* **132**, 87 (1995).
- [120] G. Steinle-Neumann, R. E. Cohen, and L. Stixrude, *J. Phys.: Condens. Matter* **16**, S1109 (2004).
- [121] K. Momma and F. Izumi, *J. Appl. Crystallogr.* **44**, 1272 (2011).
- [122] A. S. Mikhaylushkin, S. I. Simak, L. Dubrovinsky, N. Dubrovinskaia, B. Johansson, and I. A. Abrikosov, *Phys. Rev. Lett.* **99**, 165505 (2007).
- [123] A. Glensk, B. Grabowski, T. Hickel, and J. Neugebauer, *Phys. Rev. X* **4**, 011018 (2014).
- [124] Y. Gong, B. Grabowski, A. Glensk, F. Kormann, J. Neugebauer, and R. C. Reed, *Phys. Rev. B* **97**, 214106 (2018).
- [125] V. V. Kechin, *Phys. Rev. B* **65**, 052102 (2001).
- [126] T. D. Cuong and A. D. Phan, *Vacuum* **189**, 110231 (2021).
- [127] Q. J. Hong, S. V. Ushakov, A. van de Walle, and A. Navrotsky, *Proc. Natl. Acad. Sci. USA* **119**, e2209630119 (2022).
- [128] G. Aquilanti, A. Trapananti, A. Karandikar, I. Kantor, C. Marini, O. Mathon, S. Pascarelli, and R. Boehler, *Proc. Natl. Acad. Sci. USA* **112**, 12042 (2015).
- [129] A. Basu, M. R. Field, D. G. McCulloch, and R. Boehler, *Geosci. Front.* **11**, 565 (2020).
- [130] G. Morard, S. Boccato, A. D. Rosa, S. Anzellini, F. Miozzi, L. Henry, G. Garbarino, M. Mezouar, M. Harmand, F. Guyot, E. Boulard, I. Kantor, T. Irifune, and R. Torchio, *Geophys. Res. Lett.* **45**, 11074 (2018).
- [131] M. Hou, J. Liu, Y. Zhang, X. Du, H. Dong, L. Yan, J. Wang, L. Wang, and B. Chen, *Geophys. Res. Lett.* **48**, e2021GL095739 (2021).
- [132] J. M. Jackson, W. Sturhahn, M. Lerche, J. Zhao, T. S. Toellner, E. E. Alp, S. V. Sinogeikin, J. D. Bass, C. A. Murphy, and J. K. Wicks, *Earth Planet. Sci. Lett.* **362**, 143 (2013).
- [133] D. Zhang, J. M. Jackson, J. Zhao, W. Sturhahn, E. E. Alp, M. Y. Hu, T. S. Toellner, C. A. Murphy, and V. B. Prakapenka, *Earth Planet. Sci. Lett.* **447**, 72 (2016).
- [134] S. Anzellini, A. Dewaele, M. Mezouar, P. Loubeyre, and G. Morard, *Science* **340**, 464 (2013).
- [135] J. Li, Q. Wu, J. Li, T. Xue, Y. Tan, X. Zhou, Y. Zhang, Z. Xiong, Z. Gao, and T. Sekine, *Geophys. Res. Lett.* **47**, e2020GL087758 (2020).
- [136] S. J. Turneure, S. M. Sharma, and Y. M. Gupta, *Phys. Rev. Lett.* **125**, 215702 (2020).

- [137] D. Alfe, G. D. Price, and M. J. Gillan, *Phys. Rev. B* **65**, 165118 (2002).
- [138] T. Sun, J. P. Brodholt, Y. Li, and L. Vocablo, *Phys. Rev. B* **98**, 224301 (2018).
- [139] D. Alfe, *Phys. Rev. B* **79**, 060101(R) (2009).
- [140] E. Sola and D. Alfe, *Phys. Rev. Lett.* **103**, 078501 (2009).
- [141] Z. Zhang, G. Csanyi, and D. Alfe, *Geochim. Cosmochim. Acta* **291**, 5 (2020).
- [142] Y. Wang, R. Ahuja, and B. Johansson, *Phys. Rev. B* **65**, 014104 (2001).
- [143] L. Burakovsky, D. L. Preston, and R. R. Silbar, *J. Appl. Phys.* **88**, 6294 (2000).
- [144] Q. Li, J. W. Xian, Y. Zhang, T. Sun, and L. Vocablo, *J. Geophys. Res. Planets* **127**, e2021JE007015 (2022).
- [145] B. A. Buffett, *Science* **288**, 2007 (2000).
- [146] C. Davies, M. Pozzo, D. Gubbins, and D. Alfe, *Nat. Geosci.* **8**, 678 (2015).
- [147] M. Landeau, A. Fournier, H. C. Nataf, D. Cebon, and N. Schaeffer, *Nat. Rev. Earth Environ.* **3**, 255 (2022).
- [148] A. S. Côté, L. Vocablo, D. P. Dobson, D. Alfe, and J. P. Brodholt, *Phys. Earth Planet. Inter.* **178**, 2 (2010).
- [149] See Supplemental Material at <http://link.aps.org/supplemental/10.1103/PhysRevB.108.134111> for our classical MD computations at Jupiter's central pressure. It includes Refs. [81–85,134,137,139].
- [150] S. J. Bolton, A. Adriani, V. Adumitroaie, M. Allison, J. Anderson, S. Atreya, J. Bloxham, S. Brown, J. E. P. Connerney, E. DeJong, W. Folkner, D. Gautier, D. Grassi, S. Gulkis, T. Guillot, C. Hansen, W. B. Hubbard, L. Iess, A. Ingersoll, M. Janssen *et al.* *Science* **356**, 821 (2017).
- [151] A. Dewaele, P. Loubeyre, F. Occelli, M. Mezouar, P. I. Dorogokupets, and M. Torrent, *Phys. Rev. Lett.* **97**, 215504 (2006).
- [152] M. Harmand, A. Ravasio, S. Mazevet, J. Bouchet, A. Denoëud, F. Dorchie, Y. Feng, C. Fourment, E. Galtier, J. Gaudin, F. Guyot, R. Kodama, M. Koenig, H. J. Lee, K. Miyanishi, G. Morard, R. Musella, B. Nagler, M. Nakatsutsumi, N. Ozaki *et al.* *Phys. Rev. B* **92**, 024108 (2015).
- [153] T. Sjöström and S. Crockett, *Phys. Rev. E* **97**, 053209 (2018).
- [154] C. J. Wu, L. X. Benedict, P. C. Myint, S. Hamel, C. J. Prisbrey, and J. R. Leek, *Phys. Rev. B* **108**, 014102 (2023).
- [155] Y. Ping, F. Coppari, D. G. Hicks, B. Yaakobi, D. E. Fratanduono, S. Hamel, J. H. Eggert, J. R. Rygg, R. F. Smith, D. C. Swift, D. G. Braun, T. R. Boehly, and G. W. Collins, *Phys. Rev. Lett.* **111**, 065501 (2013).
- [156] R. Torchio, F. Occelli, O. Mathon, A. Sollier, E. Lescoute, L. Videau, T. Vinci, A. Benuzzi-Mounaix, J. Headspith, W. Helsby, S. Bland, D. Eakins, D. Chapman, S. Pascarelli, and P. Loubeyre, *Sci. Rep.* **6**, 26402 (2016).
- [157] J. M. Brown and R. G. McQueen, *J. Geophys. Res. Solid Earth* **91**, 7485 (1986).
- [158] Y. Huang, M. Hou, B. Gan, X. Li, D. He, G. Jiang, Y. Zhang, and Y. Liu, *J. Geophys. Res. Solid Earth* **127**, e2021JB023645 (2022).
- [159] J. H. Nguyen and N. C. Holmes, *Nature (London)* **427**, 339 (2004).
- [160] L. E. Hansen, D. E. Fratanduono, S. Zhang, D. G. Hicks, T. Suer, Z. K. Sprowal, M. F. Huff, X. Gong, B. J. Henderson, D. N. Polsin, M. Zaghoo, S. X. Hu, G. W. Collins, and J. R. Rygg, *Phys. Rev. B* **104**, 014106 (2021).
- [161] R. F. Smith, J. H. Eggert, R. E. Rudd, D. C. Swift, C. A. Bolme, and G. W. Collins, *J. Appl. Phys.* **110**, 123515 (2011).
- [162] G. R. Fowles, *J. Appl. Phys.* **32**, 1475 (1961).
- [163] D. H. Kalantar, J. F. Belak, G. W. Collins, J. D. Colvin, H. M. Davies, J. H. Eggert, T. C. Germann, J. Hawreliak, B. L. Holian, K. Kadau, P. S. Lomdahl, H. E. Lorenzana, M. A. Meyers, K. Rosolankova, M. S. Schneider, J. Sheppard, J. S. Stolken, and J. S. Wark, *Phys. Rev. Lett.* **95**, 075502 (2005).
- [164] B. Yaakobi, T. R. Boehly, D. D. Meyerhofer, T. J. B. Collins, B. A. Remington, P. G. Allen, S. M. Pollaine, H. E. Lorenzana, and J. H. Eggert, *Phys. Rev. Lett.* **95**, 075501 (2005).